Carbon Trends 16 (2024) 100387

Contents lists available at ScienceDirect

Carbon Trends

journal homepage: www.elsevier.com/locate/cartre

State change of Na clusters in hard carbon electrodes and increased capacity for Na-ion batteries achieved by heteroatom doping

Hideka Ando [a,d], Kenjiro Hashi [b], Shinobu Ohki [b], Yoshikiyo Hatakeyama [c], Yuta Nishina [a], Norihiro Kowata [a], Takahiro Ohkubo [a], Kazuma Gotoh [d,*]

[a] Graduate School of Natural Science & Technology, Okayama University, 3-1-1 Tsushima-naka, Okayama 700-8530, Japan
[b] National Institute for Materials Science, 3-13 Sakura, Tsukuba, Ibaraki 305-0003, Japan
[c] Graduate School of Science and Technology, Gunma University, 1-5-1 Tenjincho, Kiryu, Gunma 376-8515, Japan
[d] Center for Nano Materials and Technology (CNMT), Japan Advanced Institute of Science and Technology (JAIST), 1-1 Asahidai, Nomi, Ishikawa 923-1292, Japan

ARTICLE INFO

Keywords:
Sodium-ion battery
Anode material
Hard carbon
Heteroatom doping
Solid-state nuclear magnetic resonance
Sodium cluster

ABSTRACT

Although heteroatom doping is an effective method to improve the capacity of hard carbon (HC) anodes in Na-ion batteries (NIBs), the complicated structure of HC leads to uncertainty when understanding the effects of heteroatom doping on sodium storage. This study shows the effects of phosphorus and sulfur doping to HC on sodium storage using solid-state NMR to improve the capacity of HC prepared by the carbonization of resorcinol formaldehyde (RF) resin at 1100 °C. Heteroatom doping increased the battery capacity of the HC, especially the plateau capacity, but the interlayer distance of the carbon layers in the HC did not expand considerably. ^{23}Na solid-state NMR revealed that heteroatom doping facilitates the formation of quasi-metallic sodium clusters, thereby contributing to the plateau capacity increase. The metallicity of the sodium clusters in heteroatom-doped HC samples was controlled by the amount of doped-phosphorous. XPS and ^{31}P NMR detected various phosphorus sites such as phosphine and phosphine oxide in the carbon structure.

1. Introduction

Na-ion batteries (NIBs) are promising next-generation batteries that are expected to replace or complement Li-ion batteries (LIBs) because of the abundance of sodium on Earth [1,2]. Moreover, NIBs obviate the need for expensive materials such as cobalt and copper. Additionally, because of the similarity in working principles and components between NIBs and LIBs, the existing equipment and knowledge used for LIBs are applicable to NIBs with minor modifications. The electrochemical properties of various carbon materials as NIB anodes have been evaluated. Although graphite, which is commonly used as an anode material in LIBs, allows stoichiometric intercalation of sodium only up to NaC_{64}, its potential as the NIB anode has been recognized via the use of a solvent co-intercalation mechanism [3,4]. Disordered carbon materials, especially hard carbon (HC), have also been investigated as new anode materials for NIBs. Stevens and Dahn first reported a half cell using glucose-derived HC exhibiting a reversible capacity of 300 mAh g^{-1} in 2000 [5]. Our group achieved stable cycle performance by a full cell combining HC and $NaNi_{0.5}Mn_{0.5}O_2$ operating in propylene carbonate electrolyte solution [6]. Despite the proposal of various anode materials for NIBs, practical NIBs remain under development because of the need for balanced performance.

Synthesis conditions of HC play a fundamentally important role in NIB performance. Generally, HC is synthesized by carbonizing organic precursors under an inert atmosphere. Earlier works have found a relation between the carbonization temperature and the performance of HC as anodes [7–9]. They suggest that HC carbonized at 1400–1600 °C is suitable for obtaining the highest capacity in NIBs because of its balanced structure, which includes a large interlayer distance and optimal size of internal pores. Our group also reported that sucrose-derived HC carbonized at 1600 °C showed the highest capacity of 302 mAh g^{-1} [10].

However, the optimal carbonization temperature of HC for NIBs, which is higher than that of HC for LIBs (1100–1200 °C), remains problematic. In fact, higher temperatures are undesirable because of the high production costs associated with heating processes. Doping of heteroatoms (e.g., nitrogen, sulfur, and phosphorus) into HC is a promising method to increase capacity without high-temperature

* Corresponding author.
E-mail address: kgotoh@jaist.ac.jp (K. Gotoh).

https://doi.org/10.1016/j.cartre.2024.100387
Received 22 July 2024; Accepted 26 July 2024
Available online 27 July 2024

carbonization [11–25]. In some carbons, heteroatom doping induces changes in the HC structure such as the interlayer distance, pore volume, and the number of defect sites. Phosphorus-doped carbons reduce the diffusion barrier of sodium because of expansion of the interlayer space between the carbon layers [26–29]. Sulfur doping also enlarges the interlayer distance of carbon because of the large radius of sulfur atoms, thereby increasing the battery capacity [29–32]. Biomass materials have often been preferred as precursors for heteroatom-doped HC because of the efficient use of natural resources [33–44]. Also, the mechanisms underlying the increase of capacity by heteroatom doping of these materials have been investigated. However, the complicated and inhomogeneous chemical composition of the carbon materials produced from biomass, which contains plural heteroatoms and impurities, makes it difficult to clarify the effects of the heteroatoms. A systematic analysis of the effect of heteroatoms must be conducted.

Usually, HC exhibits two processes during electrochemical sodiation and desodiation: a primal slope region above 0.1 V and a following plateau region below 0.1 V for sodiation [45–48]. The high plateau capacity is beneficial for achieving high energy density. Sodium storage mechanisms in the slope region and the plateau region have been discussed in reports of numerous studies [6,29,49–58]. Some groups such as Stratford et al. [59–61] and our group [62,63] have used ^{23}Na solid-state NMR to observe the formation of quasi-metallic sodium cluster in pores near 0 V, at the last phase of the plateau region. Recently, the sodium cluster has been also investigated by Raman spectroscopy, electron paramagnetic resonance, and calculation [64–66]. Iglesias et al. have provided insight into the sodium pore-filling process for different HC microstructures such as the pore size and defect concentration by multimodal approach [67]. Controlling the formation of the closed pores suitable for cluster formation is expected to increase the plateau capacity. In fact, pore-size-controlled HC synthesized using the MgO-template method exhibits high plateau capacity and an intense ^{23}Na NMR signal, which is assigned to quasi-metallic sodium [68]. The increase in the plateau capacity has also been observed by doping heteroatoms [27,69,70]. The doped heteroatoms likely affect sodium storage in pores, especially cluster formation, although the effects of doped heteroatoms have not been evaluated in detail. Direct observation of sodium in heteroatom-doped HC can contribute to elucidation of the effects of heteroatoms on enhancing the plateau capacity.

For this study using solid-state NMR, we try to ascertain the effects of heteroatom doping into HC on sodium storage. To investigate the effects of phosphorus doping, phosphorus-doped HC samples with different dopant amounts were prepared from resorcinol-formaldehyde (RF) resin using carbonization at 1100 °C. The prepared HC samples were analyzed using techniques such as X-ray photoelectron spectroscopy (XPS), powder X-ray diffraction (PXRD), and small-angle X-ray scattering (SAXS). Additionally, ^{31}P MAS NMR was applied to reveal the structure of phosphorus doping sites. The storage state of sodium in phosphorus-doped HC samples was evaluated using ^{23}Na MAS NMR. Sulfur-doped HC samples were also evaluated for comparison with phosphorous-doped HC samples.

2. Methods

2.1. Synthesis of HC samples

An undoped HC sample was synthesized by carbonizing RF resin. In a typical preparation, 4.15 g of resorcinol was dissolved in 1.0 mL of ethanol and 6.8 mL of 0.01 M hydrochloric acid. Subsequently, 5.0 mL of formalin was added to the solution at 0 °C in an ice-water bath. After thorough mixing, the solution was placed at 40 °C in an oil bath for 24 h, followed by a temperature increase to 80 °C. It was kept at that temperature for 24 h. After the obtained product was washed three times with ethanol at 60 °C every 4 h, it was dried. The obtained RF resin was milled with a mortar. Subsequently, it was carbonized at 1100 °C with a heating rate of 10 °C min^{-1}, maintaining the temperature for 1 h in a flowing nitrogen atmosphere (500 mL min^{-1}). The resultant undoped HC was designated as RF11. (Scheme 1)

Phosphorus-doped HC samples were synthesized using a similar method to that for RF11 with the addition of phosphoric acid. For phosphorus doping, 4.0 mL of 1, 3, 5, or 7 M phosphoric acid was added to 6.8 mL of 0.01 M hydrochloric acid solution, which contains 4.15 g of resorcinol and 1.0 mL of ethanol. The molar ratios of phosphoric acid and resorcinol in the respective solutions correspond to 0.1:1, 0.3:1, 0.5:1, and 0.7:1. The resulting mixtures were polymerized and carbonized using the same process as RF11. Additionally, sulfur-doped HC samples of two types were synthesized using sulfuric acid instead of phosphoric acid, with the molar ratios of 0.1:1, and 0.3:1. The phosphorous-doped HC samples are denoted as 0.1PRF11, 0.3PRF11, 0.5PRF11, and 0.7PRF11, whereas the sulfur-doped HC samples are 0.1SRF11 and 0.3SRF11, arranged in ascending order of the dopant addition amount. 0.5SRF11 and 0.7SRF11 were also prepared, but these samples exhibited similar morphology and battery performance as 0.3SRF11. Therefore, only 0.1SRF11 and 0.3SRF11 samples are discussed for the sulfur-doped HCs in the following.

2.2. Characterization

The morphology and elemental mapping of undoped and phosphorus-doped resins were obtained using a scanning electron microscope (SEM, TM3030Plus; Hitachi High-Tech Corp.) equipped with an energy dispersive X-ray Spectrometer (EDS). The chemical compositions of the HC samples were measured using elemental analysis for hydrogen, carbon, phosphorus, and sulfur. Because the raw materials for the RF resins contain only hydrogen, carbon, phosphorus or sulfur, oxygen, and a trace amount of chlorine, the value of 100 minus the amount of hydrogen, carbon, phosphorus, and sulfur is considered to be the amount of oxygen. The Brunauer–Emmett–Teller (BET) specific surface area (SSA) of each sample was calculated using the nitrogen adsorption–desorption isotherms with a multi-point method (Belsorp-mini II; MicrotracBEL Corp.). Before BET SSA measurement, the samples were heated to 300 °C for 5 h to remove physisorbed gases. The distribution of the micropores in the undoped and phosphorus-doped HC samples was analyzed by the nonlocal density functional theory (NLDFT). The state of doped phosphorus in HC samples was evaluated using XPS and solid-state ^{31}P MAS NMR. The XPS measurements were taken using a device (JPS-9030; JEOL) with an X-ray gun operating at 12 kV with emission current of 25 mA. The ^{31}P MAS NMR spectra were recorded using a spectrometer (11.7 T magnet, JNM-ECZ500R; JEOL/Oxford Instruments) at a MAS speed of 7 kHz. We used 85 % H_3PO_4 aqueous solution as a reference at 0 ppm. The PXRD patterns were collected using a diffractometer (MiniFlex600; Rigaku Corp.) with Cu Kα radiation (λ = 0.15418 nm) at 40 kV and 10 mA, using a scan rate of 5° min^{-1}. Also, SAXS experiments were performed using the apparatus at the BL-6A station of the Photon Factory (PF) operated at 2.5 GeV and 450 mA in the Institute of Materials Structure Science, High Energy Accelerator Research Organization (KEK), Tsukuba, Japan [71,72]. The X-ray beam generated by bending magnet was monochromatized to $\lambda = 0.15$ nm and was focused to 0.5 × 0.3 mm^2 at the sample. Software developed at PF, SAngler, was used to convert 2D scattering data into 1D [73]. The X-ray profiles from the empty sample holder and glass-like carbon SRM 3600 were used to eliminate the background intensity and to normalize the SAXS intensity to absolute intensity [74,75]. In SAXS analysis, curve fitting using theoretical scattering curves was performed, assuming that the pores are spherical and that their size distribution is described by a gamma distribution. In the case of powder samples, the interstitial spaces within the sample also act as scatterers. For this reason, the analysis was conducted in a region where the scattering parameter exceeds 2 nm^{-1}, where contributions from scatterings other than micropores are minimized.

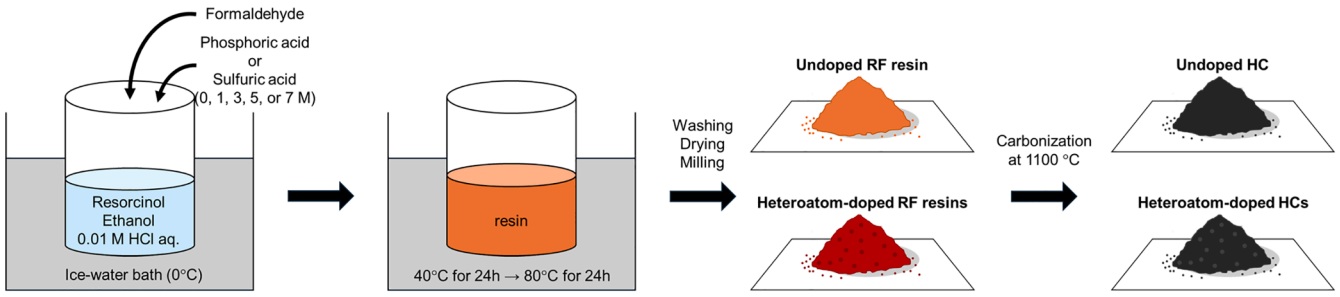

Scheme 1. Schematic illustration of the synthesis of the undoped and heteroatom-doped HC samples.

2.3. Electrochemical measurements

The electrochemical properties of the undoped and heteroatom-doped HC samples were evaluated using CR2032 coin cells assembled in an argon-filled glove box. The anodes were composed of HC as active materials, carbon black (VALCAN XC72R; Cabot Corp.), and polyimide binder (Dreambond; Industrial Summit Technology Corp.) in a weight ratio of 8:1:1. Slurry, formed by mixing these components and N-methyl-2-pyrrolidone (NMP), was coated to 100 μm thickness using the doctor blade method on aluminum or copper foil. The working electrodes were dried at 120 °C for over 15 min under vacuum and were then punched out with 15.95 mm diameter. The counter electrode was sodium metal. The electrolyte solution consisted of 1.0 M $NaPF_6$ in ethylene carbonate (EC) / diethyl carbonate (DEC) (1:1 v/v%). Galvanostatic charge–discharge tests were conducted (HJ1001-SD8; Hokuto Denko Corp.) in a range of potentials of 0.0–2.0 V (vs. Na^+/Na) at a current rate of 25 mA g^{-1}. At least three cells were assembled for each HC. Their charge–discharge capacities were evaluated.

2.4. NMR evaluation of the sodium state stored in hard carbon

The state of sodium in undoped and heteroatom-doped HC samples was analyzed using ^{23}Na MAS NMR and ^{31}P MAS NMR. Initially, sodiated HC samples were prepared electrochemically. The coin cells were assembled and subjected to a galvanostatic discharge–charge cycle ranging from 0.0 to 2.0 V at 25 mA g^{-1}. Subsequently, they were discharged to 0.2 mV at 25 mA g^{-1} and maintained at 0.2 mV until the current reached 0.25 mA g^{-1}. The discharged coin cells were disassembled in an argon-filled glove box. The anode materials, after washing with dimethyl carbonate (DMC), were scraped from the negative electrode collector, and were placed into ϕ3.2 or 4 mm NMR sample rotors with polyvinylidene fluoride (PVDF) powder. Then, using a spectrometer (11.7 T magnet, DD2 NMR; Agilent Technologies Inc.), ^{23}Na MAS NMR spectra of the undoped and phosphorous-doped HC samples were recorded. Those of the sulfur-doped HC samples were measured using a spectrometer (11.7 T magnet, AVANCE III NMR; Bruker Biospin Corp.). The RIDE pulse sequence with pulse length of 3.0 μs, a recycle delay of 0.1 s, 5000 scans, and MAS speed of 12 kHz was applied. 1 M NaCl aqueous solution was used as a reference at 0 ppm. ^{31}P MAS NMR spectra of 0.1PRF11 samples discharged to 0 V and charged to 2 V were measured using a spectrometer (11.7 T magnet, AVANCE III NMR; Bruker Biospin Corp.). The single pulse sequence with pulse length of 3.75 μs, a recycle delay of 30 s, and MAS speed of 7 kHz was applied. 85 % H_3PO_4 aqueous solution was used as a reference at 0 ppm.

3. Results and discussion

3.1. Characterization

The morphology of prepared resins is shown in Fig. S1. The undoped resin sample had irregularly shaped particles, but the 0.1PRF resin had a morphology resembling a series of spherical particles of approximately 10 μm in diameter, while the 0.3PRF, 0.5PRF, and 0.7PRF resins had almost completely spherical particles of 2–7 μm diameter. As shown in Fig. S2, the EDS mapping of the phosphorus-doped resins confirmed that phosphorus was uniformly present inside the resins. These results indicate that phosphorus is incorporated into the resins during the synthesis process and that the doped phosphorus modifies the structure of the resins. The percentage of carbon, oxygen, and phosphorus in the phosphorus-doped resins evaluated by EDS elemental analysis is shown in Table S1. Aluminum was also observed in these resins, possibly originating from the carbon tape (background). Therefore, the content of each element may not be the correct absolute value, but there is no doubt that phosphorus is present in the resins and that the phosphorus content increases with the amount of phosphoric acid added.

The percentage of elements and the results of the nitrogen adsorption–desorption method of the undoped and phosphorus-doped HC samples are presented in Table 1 and Fig. S3. Elemental analysis showed that all phosphorus-doped HC samples contained phosphorous. From RF11 to 0.3PRF11, the percentage of phosphorus increased to 1.8 wt.% with the increase in phosphoric acid. However, further addition of phosphoric acid caused little change in the doped phosphorus. 0.1PRF11 had the lowest BET SSA and open pore volume among undoped and phosphorus-doped HC samples. 0.3PRF11 and 0.5PRF11 showed almost the same BET SSA as RF11, and the pore distribution of 0.3PRF11 and 0.5PRF11 was also almost the same as RF11 except for the 2.5–3 μm sized pores. 0.7PRF11 had the highest BET SSA and open pore volume. In the case of sulfur-doped HC samples, 0.1SRF11 and 0.3SRF11 showed similar sulfur doping levels (Table S2). These results suggest that the HC synthesized using this method has an upper limit for the number of heteroatom doping sites. The excess heteroatoms are emitted as gases during carbonization, thereby forming many defects and open pores [20, 28].

To evaluate the state of phosphorus in HC samples, XPS and ^{31}P MAS NMR measurements were taken. The XPS spectra of the P 2p region of the phosphorus-doped HC samples and the ^{31}P MAS NMR spectra of phosphorus-doped HC samples are presented respectively in Fig. 1(a–d) and Fig. 1(e). The P 2p peaks of all samples (Fig. 1(a–d)) were deconvoluted into three peaks at 131.4, 133.0, and 134.8 eV, and were assigned respectively to phosphine (PR_3) or alkoxy phosphine (R_2POR'), phosphine oxide ($R_3P=O$) or phosphinic acid (R_2POOH), and phosphate ($ROP(=O)(OH)_2$) or phosphonic acid ($RP(=O)(OH)_2$) [76]. The

Table 1
Results of elemental analysis and BET SSA measurements of the undoped and phosphorus-doped HC samples. *) The wt.% of oxygen was estimated by subtracting the amount of hydrogen, carbon, and phosphorus from 100 %.

	Elemental analysis (wt.%)				BET surface area (m^2 g^{-1})
	C	H	O	P	
RF11	87.2	1.1	11.7	–	609
0.1PRF11	79.7	1.6	17.6	1.1	421
0.3PRF11	76.0	1.9	20.3	1.8	618
0.5PRF11	74.9	2.0	21.2	1.9	673
0.7PRF11	72.8	2.4	22.9	1.9	855

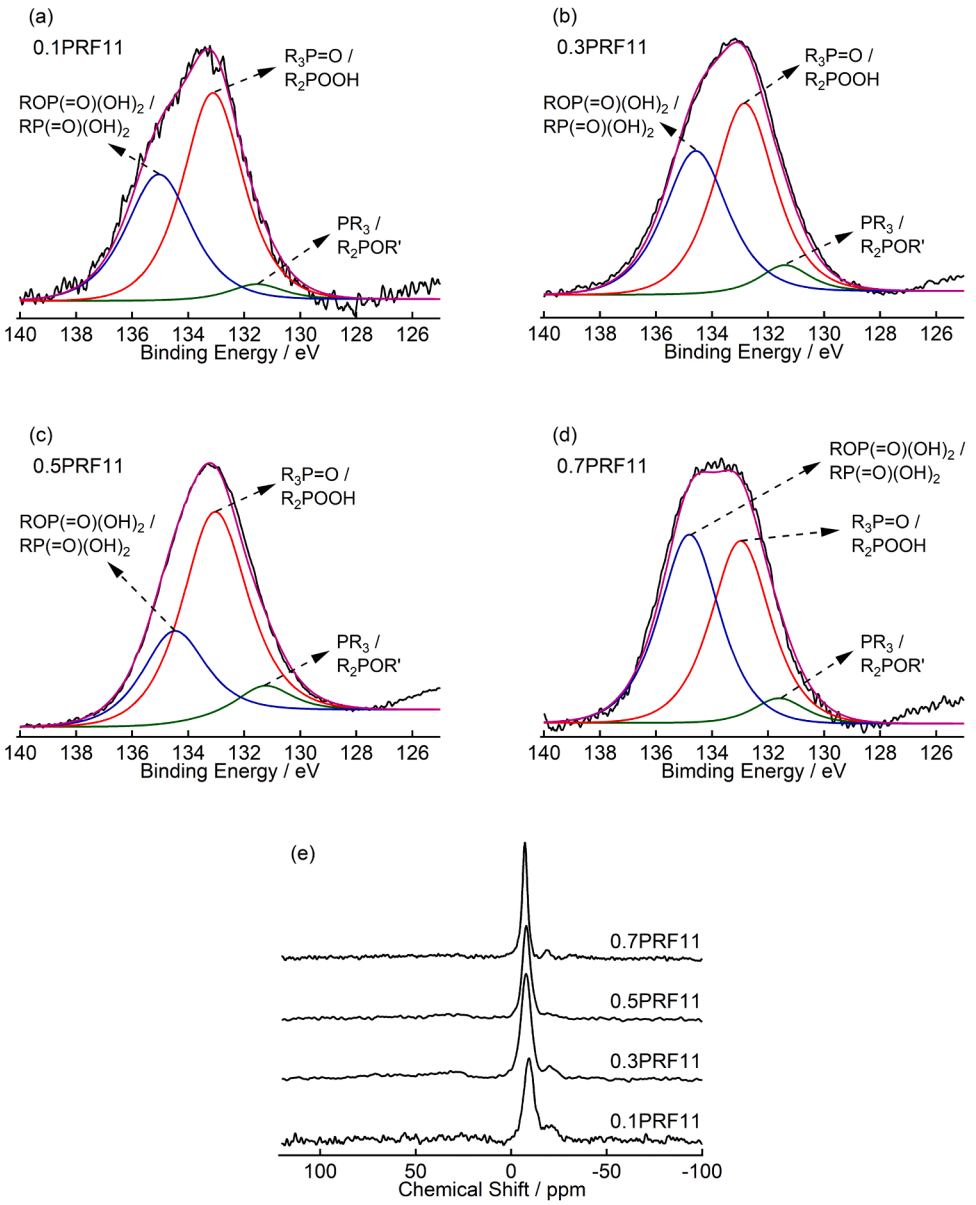

Fig. 1. High-resolution XPS spectra of the P 2p region of (a) 0.1PRF11, (b) 0.3PRF11, (c) 0.5PRF11, and (d) 0.7PRF11, and (e) ^{31}P MAS NMR spectra of phosphorus-doped HC. (For interpretation of the references to color in this figure legend, the reader is referred to the web version of this article.)

NMR spectra of all P-doped HC samples showed a major peak at −9 ppm and a small peak at −20 ppm. Although accurate assignment of these peaks is difficult because of the complicated structure of the HC, the electron density around phosphorus is expected because of a tendency for chemical shifts in organic compounds. For trivalent phosphorus, the chemical shift of phosphorus in $P(C_6H_5)_3$ is −6 ppm, whereas the chemical shift of $P(OC_6H_5)_3$ appears at the high-frequency side at 127 ppm. For pentavalent phosphorus, the chemical shift of $PO(OC_6H_5)_3$ is −18 ppm, whereas the chemical shift of $(C_6H_5)_3P=O$ is 27 ppm [77]. Therefore, the NMR peaks of the HC samples at −9 and −20 ppm are likely to be assignable respectively to PR_3 and $PO(OR)_3$. Additionally, the ^{31}P NMR spectra of some phosphorus-doped HC samples showed a very broad and negligible signal near 30 ppm. This signal might represent an overlapping of various phosphorus signals with positive chemical shifts such as $R_3P=O$ and $R_2P=O(OR)$, indicating the presence of slight phosphorus in various states. Although XPS has been used widely for evaluating phosphorus-doped HC in many studies, including our experiment, the results of NMR apparently differ from those of XPS. This discrepancy is explainable by the fact that each method observes different parts of the samples: XPS can only observe the surface of HC particles, whereas the NMR signal is obtained from the entire sample including the surface and internal structure. Therefore, the NMR measurements indicate the presence of many PR_3 species in bulk, which differs from the phosphorus species present on the surface, as revealed by XPS. Hasegawa *et al.* reported that most phosphorus atoms doped in RF resin-derived activated carbon are oxidized to P(V) with time by reacting with oxygen and moisture [76]. However, for this study, a large amount of PR_3 species remained unoxidized, suggesting that many phosphorus sites exist between interlayers and in pore structures that are not exposed to oxygen and moisture.

PXRD patterns of the phosphorus-doped HC samples are presented in Fig. 2(a). The PXRD patterns of all samples showed two broad diffraction peaks at 2θ = 15–27° and 40–48°, which were assigned respectively to the 002 and the 10 Bragg diffractions of graphite. The interlayer distances calculated from 002 peaks were 0.394, 0.397, 0.398, 0.398, and 0.402 nm, respectively, for RF11, 0.1PRF11, 0.3PRF11, 0.5PRF11, and 0.7PRF11. In fact, RF11 already had large interlayer spacing. Phosphorus doping only expanded it slightly. In addition, the pore size

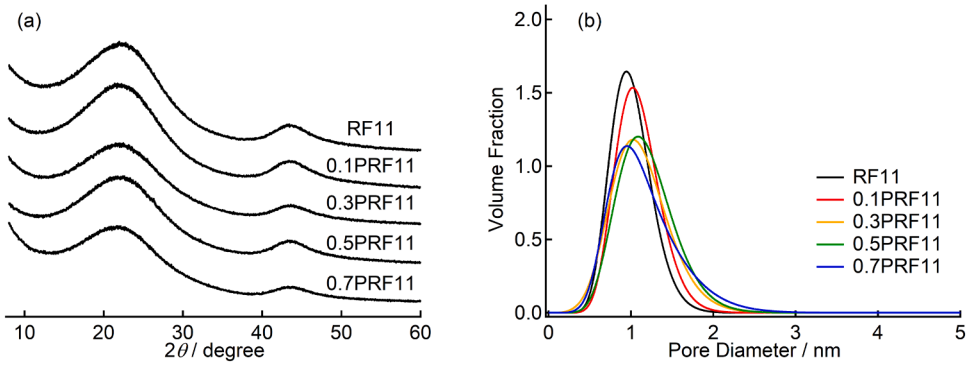

Fig. 2. (a) XRD patterns and (b) pore size distributions estimated from SAXS patterns of the undoped and phosphorus-doped HC samples. (For interpretation of the references to color in this figure legend, the reader is referred to the web version of this article.)

distribution in the HC samples was estimated using SAXS measurements to evaluate the closed pores, which cannot be assessed based on a nitrogen adsorption–desorption isotherm. Curve fitting analysis of the SAXS patterns, assuming the pores as spherical, revealed that the maximum pore size increased with added phosphorus, suggesting that phosphorus doping forms larger pores (Fig. 2(b)). Based on SAXS and nitrogen adsorption–desorption results, the number of openpores in 0.7PRF11 is higher in 0.1PRF11. The interlayer distance and pore diameter of sulfur-doped HC samples evaluated using XRD and SAXS are shown in Fig. S4. The interlayer distances for both 0.1SRF11 and 0.3SRF11 are similar to that of RF11 (Fig. S4(a)). Moreover, the pore sizes for both HC samples are almost identical (Fig. S4(b)). However, the sulfur-doped HC samples exhibited broader pore distribution peaks than the phosphorus-doped HC samples did. Several reports of earlier studies have described the increase in interlayer distance caused by heteroatom doping as a primary factor contributing to increased battery capacity [16,19,21,26–28,30,31]. However, in this study, RF11 already had a large interlayer distance. Therefore, this study's increase in battery capacity resulting from heteroatom doping should be attributed to factors other than the interlayer distance, as discussed later.

3.2. Electrochemical measurements

The electrochemical performances of the HC samples as the anode materials are shown in Fig. 3. Fig. 3 (a) shows the initial charge–discharge curves of the HC samples exhibiting capacities closest to the average value. The averaged initial charge capacities of RF11, 0.1RFF11, 0.3PRF11, 0.5PRF11, and 0.7PRF11 were, respectively, 255, 328, 310, 286, and 100 mAh g^{-1}. The capacities of 0.1PRF11, 0.3PRF11, and 0.5PRF11 show improvement compared to that of RF11. Among them, 0.1PRF11 exhibits the greatest capacity: 29 % higher than that of RF11. By contrast, the capacity of 0.7PRF11 decreased compared to that of RF11. The initial Coulombic efficiencies (ICE) of RF11, 0.1PRF11, 0.3PRF11, 0.5PRF11, and 0.7PRF11 were, respectively, 63, 71, 66, 67, and 33 %. A certain increase in the ICE of 0.1PRF11 compared to RF11 was observed, whereas 0.7PRF11 was found to have a marked decrease (Fig. 3). The lower ICE of 0.7PRF11 is mainly ascribable to the increase of specific surface area due to the increase of the number of open pores.

To elucidate changes in battery capacity, the initial charge capacities of these HC samples were divided into a slope region and a plateau region at 0.12 V, as shown in Fig. 3(b). Regarding the slope capacity, 0.1PRF11 exhibited the largest, reaching 183 mAh g^{-1}. The best electrochemical performance of 0.1PRF11 suggests that phosphorus doping has an advantage over the disadvantage caused by increased specific surface area. The slope capacities decreased with the amount of added phosphorus. The slope capacity of 0.3PRF11 was almost identical to that of RF11 (0.3PRF11:146 mAh g^{-1}, RF11:144 mAh g^{-1}). Also, both 0.5PRF11 and 0.7PRF11 showed lower slope capacities than RF11 (0.5PRF11:132 mAh g^{-1}, 0.7PRF11:78 mAh g^{-1}). The slope capacity and ICE decrease are attributable to their excessive defect sites and high specific surface area [27,78]. The plateau capacities of 0.1PRF11, 0.3PRF11, and 0.5PRF11 all improved (RF11:110 mAh g^{-1}, 0.1PRF11:145 mAh g^{-1}, 0.3PRF11:164 mAh g^{-1}, 0.5PRF11:155 mAh g^{-1}). The increased plateau capacity is attributable to their increased inserted sodium into interlayer spaces and sodium stored in pores [50,54,61,79]. It is noteworthy that the interlayer distance of RF11 was already large. The effect of heteroatom doping on the change in the interlayer spacing was small. The increased plateau capacity with no increase in interlayer distance indicates that sodium stored in the pores contributes to the increased plateau capacity. The plateau capacity of 0.7PRF11 decreased considerably (22 mAh g^{-1}), whereas the irreversible capacity of 0.7PRF11 increased compared to that of RF11. This result suggests that the excessive phosphorus addition engenders dramatic changes in the carbon morphology, leading to a decrease in

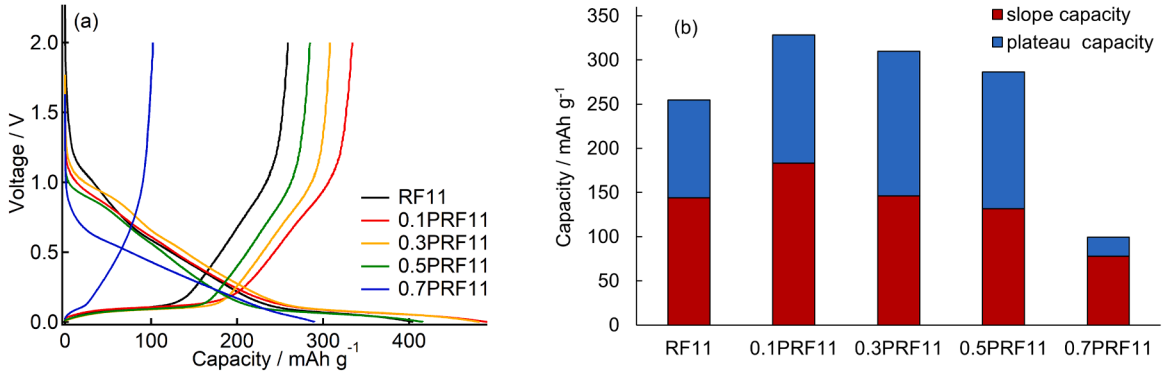

Fig. 3. (a) Initial charge–discharge profiles and (b) initial charge capacities of the slope and plateau region of the undoped and phosphorus-doped HC samples. (For interpretation of the references to color in this figure legend, the reader is referred to the web version of this article.)

sodium storage sites. It also facilitates the formation of a large amount of solid electrolyte interface (SEI) because of the increased surface area. Regarding the sulfur-doped HC samples, both HC samples (0.1SRF11 and 0.3SRF11) also exhibited improved capacities compared to RF11. The slope capacities of 0.1SRF11 and 0.3SRF11 were, respectively, 187 and 168 mAh g^{-1} (Fig. S5). Improvement in the slope capacity was likely attributable to the increase of sulfur doping sites acting as sodium storage sites, similar to the case of phosphorus doping. The plateau capacities of 0.1SRF11 and 0.3SRF11 were, respectively, 140 and 143 mAh g^{-1}. The plateau capacities were also improved compared to that of RF11, resulting from increased amounts of stored sodium in the pores, as observed for phosphorus doping.

3.3. Evaluation of the sodium state in hard carbon

The sodium in the HC samples was observed using ^{23}Na MAS NMR, as shown in Fig. 4. Each NMR spectrum showed a peak at −8 ppm, which was assigned to ionic sodium species such as residual electrolyte, SEI, and sodium inserted between layers [54,62]. Additionally, three phosphorus-doped HC samples exhibited a broad peak at 600–1000 ppm: 0.1PRF11, 0.3PRF11, and 0.5PRF11 (Fig. 4(a)). This signal, shifted to a higher frequency side because of the Knight shift, is assigned to the quasi-metallic sodium cluster, which has been reported for several HC samples prepared especially using higher carbonization temperatures [59,61,62]. Similarly, the NMR spectra of sulfur-doped HC samples, 0.1SRF11 and 0.3SRF11, exhibited a broad peak attributed to quasi-metallic sodium at 600–1100 ppm (Fig. 4(b)). However, because of the formation of many open pores resulting from the emission of excess heteroatoms as gases during the carbonization of 0.7PRF11, the NMR spectrum of 0.7PRF11 showed no distinct quasi-metallic component.

The signals of quasi-metallic sodium clusters in the phosphorus-doped HC samples shifted to a higher frequency side with more added phosphorus. In addition, the signal intensities increased with the added phosphorous (except for 0.7PRF11). However, the chemical shifts of quasi-metallic sodium formed in sulfur-doped HC samples (0.1SRF11 and 0.3SRF11) are almost constant. Fundamentally, larger closed pores in HC allow for the forming of larger sodium clusters, which are highly metallic and which give a high Knight shift value [61–63]. However, the NMR signals of the quasi-metallic sodium cluster formed in the sulfur-doped HC samples and 0.1PRF11 showed a nearly constant shift, although the sulfur-doped HC samples had larger pores than 0.1PRF11 showed. Indeed, the doping elements can also affect the sodium cluster metallicity. Stratford et al. have reported that the number of defects on the carbon surface affects the sodium cluster metallicity [60]. They suggest that carbon with defects has higher trapped electron density near the defects and a larger partial charge on the sodium ions, which leads to a smaller Knight shift. By contrast, in this study, the metallicity of sodium clusters formed in phosphorus-doped HC samples increased with added phosphorus. This phenomenon might be caused by a difference in the ease of transfer of electron density from sodium to the defect sites and from sodium to the doped heteroatoms. Because the electronegativities of phosphorus and sulfur are respectively more minor than and similar to those of carbon (C:2.55, P:2.19, and S:2.58), the defect sites with phosphorus might be favorable for the electron transfer and the formation of sodium clusters with high metallicity, whereas those with sulfur might behave similarly to defect sites without heteroatoms. We have observed that a ^{31}P MAS NMR signal of the sodiated 0.1PRF11 sample shifted to a higher frequency side compared to that of the desodiated 0.1PRF11 sample, which may be due to the decreased shielding from electrons around phosphorus (Fig. S6).

The increase in quasi-metallic Na cluster signal intensity by addition of phosphorous (Fig. 4(a)) can be attributed to an increase in the amount of quasi-metallic clusters. It is possible that the number of defect sites on the graphene surface, which are the starting point for cluster formation [66], has also increased.

3.4. Effects of heteroatom doping on sodium storage

Our experiments showed that phosphorus and sulfur doping into HC improved the electrochemical performance, especially the extension of plateau capacities. The heteroatom-doped HC samples (except for 0.7PRF11) showed more quasi-metallic sodium clusters. This observation demonstrates that the facilitation of forming quasi-metallic sodium clusters by heteroatom doping plays an important role in the increase of the plateau capacity. This facilitation of the formation of quasi-metallic sodium clusters might be attributed to the increased closed pore size and the increased number of heteroatoms doping sites in the pores, where sodium can be absorbed easily. Based on the results, a schematic diagram of the effect of heteroatom doping sites on sodium storage is shown in Fig. 5. In the sodiation process, sodium ions are inserted into interlayers and adsorbed around defects, including heteroatom doping sites, as shown in Fig. 5(b). Because the ^{31}P NMR measurements taken for this study suggest that large amounts of PR_3 species are present in the bulk of phosphorus-doped HC samples, the PR_3 species might contribute as a major sodium adsorption site in the pores. In fact, some studies have calculated the binding energies of sodium ions to phosphorus doping sites. The results demonstrate that sodium ions adsorb more easily to PR_3 species than to graphene [20,22,29]. Unfortunately, the state of sulfur in the bulk of sulfur-doped HC could not be evaluated using ^{33}S NMR because of its low sensitivity. However, the ^{23}Na NMR signal of the sodium cluster was observed clearly in sulfur-doped HC samples, suggesting that sulfur doping has some positive effects on cluster formation. Then, sodium ions are likely to gather around the heteroatom doping sites. They might grow into quasi-metallic sodium clusters with that site as a core around 0 V, as shown in Fig. 5(c). In the desodiation process, most sodium is desorbed from the HC, but some sodium remains in the HC as irreversible sodium, as shown in Fig. 5(d). In particular, 0.7PRF11

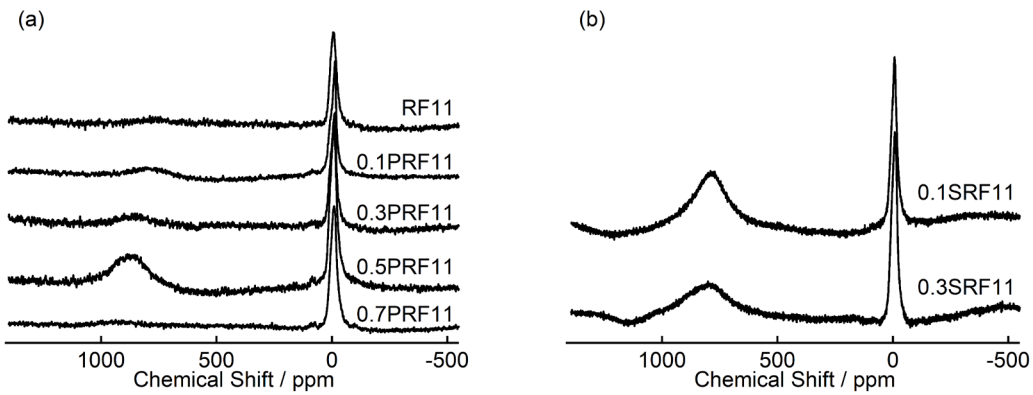

Fig. 4. ^{23}Na MAS NMR spectra of (a) undoped and phosphorus-doped HC samples and (b) sulfur-doped HC samples.

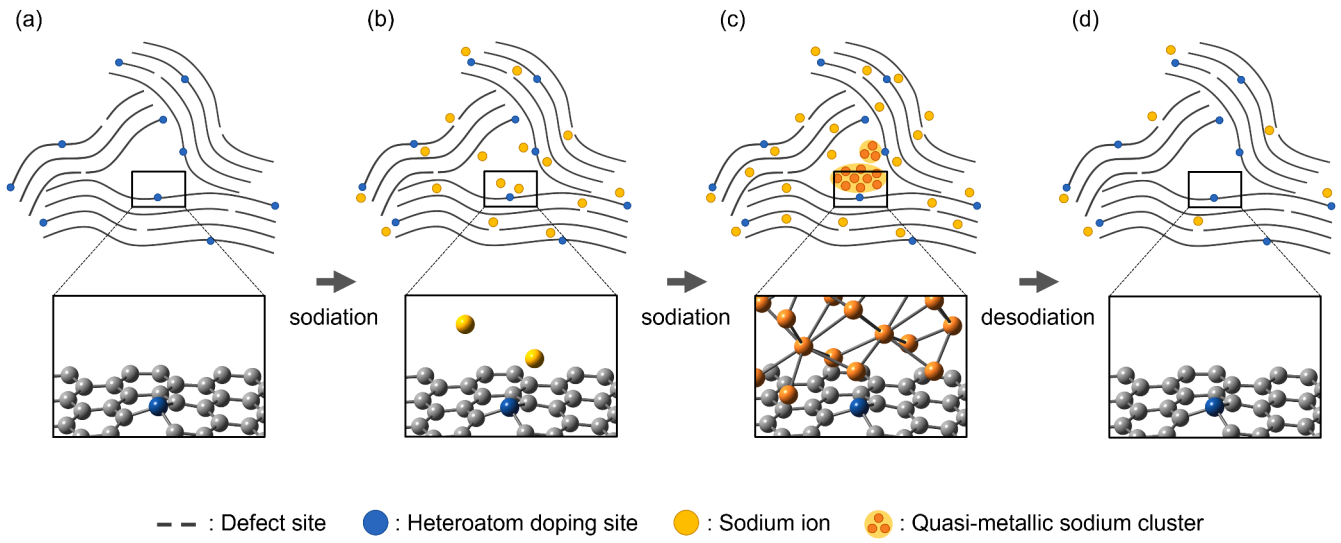

Fig. 5. Schematic diagram of sodium storage state in heteroatom-doped HC (a) before sodium storage, (b) during sodium storage, (c) during quasi-metallic sodium cluster formation at 0 V, and (d) after desodiation. (For interpretation of the references to color in this figure legend, the reader is referred to the web version of this article.)

contained a large amount of irreversible sodium. The XPS spectrum of 0.7PRF11 showed more ROP(=O)$(OH)_2$ and RP(=O)$(OH)_2$, suggesting that highly oxidized phosphorus on the edge is likely to contribute to irreversible capacity. In fact, Li et al. reported that edge-doped PC$(OH)_2$ and PCO(OH) exhibit extremely high binding energy with sodium [29]. Our results suggest that HC containing closed pores with adequate heteroatom sites can contribute to NIBs with higher energy density.

4. Conclusion

We tried to increase the plateau capacity of HC anodes by heteroatom doping without high carbonization temperatures and to investigate details of heteroatom doping effects on sodium storage. Phosphorus-doped and sulfur-doped HC samples were synthesized at 1100 °C from RF resins with different dopant amounts. Despite the low carbonization temperature of 1100 °C, which is known to be insufficient for achieving high plateau capacity, the phosphorus-doped and sulfur-doped HC samples exhibited higher plateau capacity than that found for undoped HC. The increased capacity can be attributed to the facilitation of sodium cluster formation provided by the change in pore size and the heteroatom doping sites, as evidenced by the appearance of the ^{23}Na NMR signal of the quasi-metallic sodium cluster. No marked change in the interlayer distance by heteroatom doping, which is considered the main factor for increasing capacity, was observed in the HC samples used for this study. The ^{23}Na NMR chemical shifts of the sodium cluster signals in heteroatom-doped HC samples shifted depending on the heteroatom type and amount, suggesting that the electronegativity of the doped heteroatoms influences metallicity in addition to the pore size. Regarding the phosphorus-doped HC samples, phosphorus doping sites in carbon structures such as PR_3, observed using ^{31}P NMR, might play an important role in facilitating sodium cluster formation and changing the state of the sodium cluster. The state of sulfur in the bulk of sulfur-doped HC samples has not yet been clarified, but it might exert similar positive effects on cluster formation. This study provides new insights into the effects of heteroatom-doping on HC, which are expected to be helpful for realizing high-energy anode materials at low carbonization temperatures.

CRediT authorship contribution statement

Hideka Ando: Conceptualization, Data curation, Formal analysis, Methodology, Writing – original draft. **Kenjiro Hashi:** Formal analysis, Methodology, Resources. **Shinobu Ohki:** Methodology, Resources. **Yoshikiyo Hatakeyama:** Data curation, Methodology, Writing – review & editing. **Yuta Nishina:** Methodology, Resources, Writing – review & editing. **Norihiro Kowata:** Data curation, Formal analysis, Methodology. **Takahiro Ohkubo:** Formal analysis, Methodology, Writing – review & editing. **Kazuma Gotoh:** Conceptualization, Funding acquisition, Investigation, Project administration, Supervision, Writing – review & editing.

Declaration of competing interest

The authors declare the following financial interests/personal relationships which may be considered as potential competing interests:

Kazuma Gotoh reports financial support was provided by Japan Science and Technology Agency. Kazuma Gotoh reports financial support was provided by Japan Society for the Promotion of Science. Kazuma Gotoh reports financial support was provided by Acquisition Technology and Logistics Agency. Hideka Ando reports financial support was provided by Japan Science and Technology Agency. If there are other authors, they declare that they have no known competing financial interests or personal relationships that could have appeared to influence the work reported in this paper.

Data availability

Data will be made available on request.

Acknowledgements

This work was supported by JST SPRING Grant No. JPMJSP2126, JST GteX JPMJGX23S4, JSPS KAKENHI Grant No. 23K04535, and ATLA Grant No. JPJ004596.

We are grateful to the PF Advisory Committee of KEK for approving the SAXS measurements under Proposal No. 2022G101.

The authors thank Dr. Zhou Yang (Okayama University) and Dr. Shun Nishimura (JAIST) for support with XPS measurement and nitrogen adsorption–desorption measurement, respectively.

Supplementary materials

Supplementary material associated with this article can be found, in

the online version, at doi:10.1016/j.cartre.2024.100387.

References

[1] N. Yabuuchi, K. Kubota, M. Dahbi, S. Komaba, Research development on sodium-ion batteries, Chem. Rev. 114 (2014) 11636–11682.
[2] J.-Y. Hwang, S.-T. Myung, Y.-K. Sun, Sodium-ion batteries: present and future, Chem. Soc. Rev. 46 (2017) 3529–3614.
[3] Z.T. Gossage, T. Hosaka, R. Tatara, S. Komaba, Branched diamine electrolytes for Na^+-solvent cointercalation into graphite, ACS Appl. Energy Mater. 7 (2024) 845–849.
[4] I. Escher, A.I. Freytag, J.M. López del Amo, P. Adelhelm, Solid-state NMR study on the structure and dynamics of graphite electrodes in sodium-ion batteries with solvent co-intercalation, Batteries Supercaps 6 (2023) e202200421.
[5] D.A. Stevens, J.R. Dahn, High capacity anode materials for rechargeable sodium-ion batteries, J. Electrochem. Soc. 147 (2000) 1271–1273.
[6] S. Komaba, W. Murata, T. Ishikawa, N. Yabuuchi, T. Ozeki, T. Nakayama, A. Ogata, K. Gotoh, K. Fujiwara, Electrochemical Na insertion and solid electrolyte interphase for hard-carbon electrodes and application to Na-ion batteries, Adv. Funct. Mater. 21 (2011) 3859–3867.
[7] H. Yamamoto, S. Muratsubaki, K. Kubota, M. Fukunishi, H. Watanabe, J. Kim, S. Komaba, Synthesizing higher-capacity hard-carbons from cellulose for Na- and K-ion batteries, J. Mater. Chem. A 6 (2018) 16844–16848.
[8] A. Kamiyama, K. Kubota, T. Nakano, S. Fujimura, S. Shiraishi, H. Tsukada, S. Komaba, High-capacity hard carbon synthesized from macroporous phenolic resin for sodium-ion and potassium-ion battery, ACS Appl. Energy Mater. 3 (2020) 135–140.
[9] Z. Guo, Z. Xu, F. Xie, J. Jiang, K. Zheng, S. Alabidun, M. Crespo-Ribadeneyra, Y.-S. Hu, H. Au, M.M. Titirici, Investigating the superior performance of hard carbon anodes in sodium-ion compared with lithium- and potassium-ion batteries, Adv. Mater. 35 (2023) 2304091.
[10] R. Morita, K. Gotoh, M. Fukunishi, K. Kubota, S. Komaba, N. Nishimura, T. Yumura, K. Deguchi, S. Ohki, T. Shimizu, H. Ishida, Combination of solid state NMR and DFT calculation to elucidate the state of sodium in hard carbon electrodes, J. Mater. Chem. A 4 (2016) 13183–13193.
[11] J. Song, Y. Xu, Y. Wang, S. Li, S. Yin, W. Cen, D. Xiao, Q. Zhao, X. Zhang, Y. Meng, A synthesis strategy of 3D carbon nanosheet anode with adsorption/intercalation-filling hybrid mechanism for high-performance sodium/potassium-ion batteries, Appl. Surf. Sci. 657 (2024) 159770.
[12] H. Liu, M. Jia, N. Sun, B. Cao, R. Chen, Q. Zhu, F. Wu, N. Qiao, B. Xu, Nitrogen-rich mesoporous carbon as anode material for high-performance sodium-ion batteries, ACS Appl. Mater. Interfaces 7 (2015) 27124–27130.
[13] J. Zhu, C. Chen, Y. Lu, Y. Ge, H. Jiang, K. Fu, X. Zhang, Nitrogen-doped carbon nanofibers derived from polyacrylonitrile for use as anode material in sodium-ion batteries, Carbon N. Y. 94 (2015) 189–195.
[14] S. Huang, Z. Li, B. Wang, J. Zhang, Z. Peng, R. Qi, J. Wang, Y. Zhao, N-doping and defective nanographitic domain coupled hard carbon nanoshells for high performance lithium/sodium storage, Adv. Funct. Mater. 28 (2018) 1706294.
[15] G. Huang, Q. Kong, W. Yao, Q. Wang, High proportion of active nitrogen-doped hard carbon based on mannich reaction as anode material for high-performance sodium-ion batteries, ChemSusChem 16 (2023) e202202070.
[16] W. Li, M. Zhou, H. Li, K. Wang, S. Cheng, K. Jiang, A high performance sulfur-doped disordered carbon anode for sodium ion batteries, Energy Environ. Sci. 8 (2015) 2916–2921.
[17] T. Chen, J. Wu, X. Zhang, X. Han, S. Liu, J. Yang, Pseudocapacitive contribution in sulfur-doped porous carbon nanosheets enables high-performance sodium-ion storage, Carbon N. Y. 227 (2024) 119276.
[18] J. Tzadikov, N.R. Levy, L. Abisdris, R. Cohen, M. Weitman, I. Kaminker, A. Goldbourt, Y. Ein-Eli, M. Shalom, Bottom-up synthesis of advanced carbonaceous anode materials containing sulfur for Na-ion batteries, Adv. Funct. Mater. 30 (2020) 2000592.
[19] F. Wu, R. Dong, Y. Bai, Y. Li, G. Chen, Z. Wang, C. Wu, Phosphorus-doped hard carbon nanofibers prepared by electrospinning as an anode in sodium-ion batteries, ACS Appl. Mater. Interfaces 10 (2018) 21335–21342.
[20] Y. Li, Y. Yuan, Y. Bai, Y. Liu, Z. Wang, L. Li, F. Wu, K. Amine, C. Wu, J. Lu, Insights into the Na^+ storage mechanism of phosphorus-functionalized hard carbon as ultrahigh capacity anodes, Adv. Energy Mater. 8 (2018) 1702781.
[21] Y. Qiao, R. Han, Y. Pang, Z. Lu, J. Zhao, X. Cheng, H. Zhang, Z. Yang, S. Yang, Y. Liu, 3D well-ordered porous phosphorus doped carbon as an anode for sodium storage: structure design, experimental and computational insights, J. Mater. Chem. A 7 (2019) 11400–11407.
[22] X. Wang, M. Hou, Z. Shi, X. Liu, I. Mizota, H. Lou, B. Wang, X. Hou, Regulate phosphorus configuration in high P-doped hard carbon as a superanode for sodium storage, ACS Appl. Mater. Interfaces 13 (2021) 12059–12068.
[23] J. Yan, H. Li, K. Wang, Q. Jin, C. Lai, R. Wang, S. Cao, J. Han, Z. Zhang, J. Su, K. Jiang, Ultrahigh phosphorus doping of carbon for high-rate sodium ion batteries anode, Adv. Energy Mater. 11 (2021) 2003911.
[24] S. Wu, H. Peng, L. Huang, Y. Liu, Y. Wu, L. Liu, W. Ai, Z. Sun, P-doped hard carbon microspheres for sodium-ion battery anodes with superior rate and cyclic performance, Inorg. Chem. Front. 10 (2023) 5908–5916.
[25] H. Wang, H. Yuan, W. Zhan, Y.-S. Lee, H.-J. Shin, X. Wei, Q. Cai, J.-L. Lan, Y. Yu, X. Yang, Integrated N, P co-doped and dense carbon networks produced by a chemical crosslinking strategy: facilitating high gravimetric/volumetric performance sodium ion batteries, Carbon N. Y. 165 (2020) 204–215.
[26] Z. Li, L. Ma, T.W. Surta, C. Bommier, Z. Jian, Z. Xing, W.F. Stickle, M. Dolgos, K. Amine, J. Lu, T. Wu, X. Ji, High capacity of hard carbon anode in Na-ion batteries unlocked by PO_x doping, ACS Energy Lett. 1 (2016) 395–401.
[27] S. Alvin, C. Chandra, J. Kim, Extended plateau capacity of phosphorus-doped hard carbon used as an anode in Na- and K-ion batteries, Chem. Eng. J. 391 (2020) 123576.
[28] N. Li, Q. Yang, Y. Wei, R. Rao, Y. Wang, M. Sha, X. Ma, L. Wang, Y. Qian, Phosphorus-doped hard carbon with controlled active groups and microstructure for high-performance sodium-ion batteries, J. Mater. Chem. A 8 (2020) 20486–20492.
[29] Z. Li, C. Bommier, Z.S. Chong, Z. Jian, T.W. Surta, X. Wang, Z. Xing, J. C. Neuefeind, W.F. Stickle, M. Dolgos, P.A. Greaney, X. Ji, Mechanism of Na-ion storage in hard carbon anodes revealed by heteroatom doping, Adv. Energy Mater. 7 (2017) 1602894.
[30] L. Qie, W. Chen, X. Xiong, C. Hu, F. Zou, P. Hu, Y. Huang, Sulfur-doped carbon with enlarged interlayer distance as a high-performance anode material for sodium-ion batteries, Adv. Sci. 2 (2015) 1500195.
[31] G. Zou, C. Wang, H. Hou, C. Wang, X. Qiu, X. Ji, Controllable interlayer spacing of sulfur-doped graphitic carbon nanosheets for fast sodium-ion batteries, Small 13 (2017) 1700762.
[32] Z. Hong, Y. Zhen, Y. Ruan, M. Kang, K. Zhou, J.-M. Zhang, Z. Huang, M. Wei, Rational design and general synthesis of S-doped hard carbon with tunable doping sites toward excellent Na-ion storage performance, Adv. Mater. 30 (2018) 1802035.
[33] G. Xu, J. Han, B. Ding, P. Nie, J. Pan, H. Dou, H. Li, X. Zhang, Biomass-derived porous carbon materials with sulfur and nitrogen dual-doping for energy storage, Green Chem. 17 (2015) 1668–1674.
[34] T. Yang, T. Qian, M. Wang, X. Shen, N. Xu, Z. Sun, C. Yan, A sustainable route from biomass byproduct okara to high content nitrogen-doped carbon sheets for efficient sodium ion batteries, Adv. Mater. 28 (2016) 539–545.
[35] R.R. Gaddam, A.H. Farokh Niaei, M. Hankel, D.J. Searles, N.A. Kumar, X.S. Zhao, Capacitance-enhanced sodium-ion storage in nitrogen-rich hard carbon, J. Mater. Chem. A 5 (2017) 22186–22192.
[36] G. Zhao, G. Zou, H. Hou, P. Ge, X. Cao, X. Ji, Sulfur-doped carbon employing biomass-activated carbon as a carrier with enhanced sodium storage behavior, J. Mater. Chem. A 5 (2017) 24353–24360.
[37] D. Qin, Z. Liu, Y. Zhao, G. Xu, F. Zhang, X. Zhang, A sustainable route from corn stalks to N, P-dual doping carbon sheets toward high performance sodium-ion batteries anode, Carbon N. Y. 130 (2018) 664–671.
[38] C. Yang, J. Xiong, X. Ou, C.-F. Wu, X. Xiong, J.-H. Wang, K. Huang, M. Liu, A renewable natural cotton derived and nitrogen/sulfur co-doped carbon as a high-performance sodium ion battery anode, Mater. Today Energy 8 (2018) 37–44.
[39] Y. Zhu, Y. Huang, C. Chen, M. Wang, P. Liu, Phosphorus-doped porous biomass carbon with ultra-stable performance in sodium storage and lithium storage, Electrochim. Acta 321 (2019) 134698.
[40] L.A. Romero-Cano, H. García-Rosero, F. Carrasco-Marín, A.F. Pérez-Cadenas, L. V. González-Gutiérrez, A.I. Zárate-Guzmán, G. Ramos-Sánchez, Surface functionalization to abate the irreversible capacity of hard carbons derived from grapefruit peels for sodium-ion batteries, Electrochim. Acta 326 (2019) 134973.
[41] M. Khan, N. Ahmad, K. Lu, Z. Sun, C. Wei, X. Zheng, R. Yang, Nitrogen-doped carbon derived from onion waste as anode material for high performance sodium-ion battery, Solid State Ion. 346 (2020) 115223.
[42] N. Shaji, C.W. Ho, M. Nanthagopal, P. Santhoshkumar, G.S. Sim, C.W. Lee, Biowaste-derived heteroatoms-doped carbon for sustainable sodium-ion storage, J. Alloys Compd. 872 (2021) 159670.
[43] G. Zhao, D. Yu, H. Zhang, F. Sun, J. Li, L. Zhu, L. Sun, M. Yu, F. Besenbacher, Y. Sun, Sulphur-doped carbon nanosheets derived from biomass as high-performance anode materials for sodium-ion batteries, Nano Energy 67 (2020) 104219.
[44] N.T. Aristote, Z. Song, W. Deng, H. Hou, G. Zou, X. Ji, Effect of double and triple-doping of sulfur, nitrogen and phosphorus on the initial coulombic efficiency and rate performance of the biomass derived hard carbon as anode for sodium-ion batteries, J. Power Sources 558 (2023) 232517.
[45] D. Saurel, B. Orayech, B. Xiao, D. Carriazo, X. Li, T. Rojo, From charge storage mechanism to performance: a roadmap toward high specific energy sodium-ion batteries through carbon anode optimization, Adv. Energy Mater. 8 (2018) 1703268.
[46] H. Hou, X. Qiu, W. Wei, Y. Zhang, X. Ji, Carbon anode materials for advanced sodium-ion batteries, Adv. Energy Mater. 7 (2017) 1602898.
[47] X. Dou, I. Hasa, D. Saurel, C. Vaalma, L. Wu, D. Buchholz, D. Bresser, S. Komaba, S. Passerini, Hard carbons for sodium-ion batteries: structure, analysis, sustainability, and electrochemistry, Mater. Today 23 (2019) 87–104.
[48] C. Huang, J. Yin, W. Shi, Y. Cheng, X. Xu, Recent advances of tailoring defects and pores in hard carbon for sodium storage, Mater. Today Energy 40 (2024) 101501.
[49] D.A. Stevens, J.R. Dahn, The mechanisms of lithium and sodium insertion in carbon materials, J. Electrochem. Soc. 148 (2001) A803–A811.
[50] C. Bommier, T.W. Surta, M. Dolgos, X. Ji, New mechanistic insights on Na-ion storage in nongraphitizable carbon, Nano Lett. 15 (2015) 5888–5892.
[51] S. Qiu, L. Xiao, M.L. Sushko, K.S. Han, Y. Shao, M. Yan, X. Liang, L. Mai, J. Feng, Y. Cao, X. Ai, H. Yang, J. Liu, Manipulating adsorption-insertion mechanisms in nanostructured carbon materials for high-efficiency sodium ion storage, Adv. Energy Mater. 7 (2017) 1700403.
[52] P. Bai, Y. He, X. Zou, X. Zhao, P. Xiong, Y. Xu, Elucidation of the sodium-storage mechanism in hard carbons, Adv. Energy Mater. 8 (2018) 1703217.

[53] H. Lu, F. Ai, Y. Jia, C. Tang, X. Zhang, Y. Huang, H. Yang, Y. Cao, Exploring sodium-ion storage mechanism in hard carbons with different microstructure prepared by ball-milling method, Small 14 (2018) 1802694.
[54] S. Alvin, D. Yoon, C. Chandra, H.S. Cahyadi, J.-H. Park, W. Chang, K.Y. Chung, J. Kim, Revealing sodium ion storage mechanism in hard carbon, Carbon N. Y. 145 (2019) 67–81.
[55] N. Sun, Z. Guan, Y. Liu, Y. Cao, Q. Zhu, H. Liu, Z. Wang, P. Zhang, B. Xu, Extended "adsorption–insertion" model: a new insight into the sodium storage mechanism of hard carbons, Adv. Energy Mater. 9 (2019) 1901351.
[56] X. Chen, Y. Fang, J. Tian, H. Lu, X. Ai, H. Yang, Y. Cao, Electrochemical insight into the sodium-ion storage mechanism on a hard carbon anode, ACS Appl. Mater. Interfaces 13 (2021) 18914–18922.
[57] J. Han, I. Johnson, Z. Lu, A. Kudo, M. Chen, Effect of local atomic structure on sodium ion storage in hard amorphous carbon, Nano Lett. 21 (2021) 6504–6510.
[58] I.K. Ilic, K. Schutjajew, W. Zhang, M. Oschatz, Changes of porosity of hard carbons during mechanical treatment and the relevance for sodium-ion anodes, Carbon N. Y. 186 (2022) 55–63.
[59] J.M. Stratford, P.K. Allan, O. Pecher, P.A. Chater, C.P. Grey, Mechanistic insights into sodium storage in hard carbon anodes using local structure probes, Chem. Commun. 52 (2016) 12430–12433.
[60] J.M. Stratford, A.K. Kleppe, D.S. Keeble, P.A. Chater, S.S. Meysami, C.J. Wright, J. Barker, M.M. Titirici, P.K. Allan, C.P. Grey, Correlating local structure and sodium storage in hard carbon anodes: insights from pair distribution function analysis and solid-state NMR, J. Am. Chem. Soc. 143 (2021) 14274–14286.
[61] H. Au, H. Alptekin, A.C.S. Jensen, E. Olsson, C.A. O'Keefe, T. Smith, M. Crespo-Ribadeneyra, T.F. Headen, C.P. Grey, Q. Cai, A.J. Drew, M.-M. Titirici, A revised mechanistic model for sodium insertion in hard carbons, Energy Environ. Sci. 13 (2020) 3469–3479.
[62] R. Morita, K. Gotoh, K. Kubota, S. Komaba, K. Hashi, T. Shimizu, H. Ishida, Correlation of carbonization condition with metallic property of sodium clusters formed in hard carbon studied using ^{23}Na nuclear magnetic resonance, Carbon N. Y. 145 (2019) 712–715.
[63] K. Gotoh, T. Yamakami, I. Nishimura, H. Kometani, H. Ando, K. Hashi, T. Shimizu, H. Ishida, Mechanisms for overcharging of carbon electrodes in lithium-ion/sodium-ion batteries analysed by *operando* solid-state NMR, J. Mater. Chem. A 8 (2020) 14472–14481.
[64] Y. Aniskevich, J.H. Yu, J.-Y. Kim, S. Komaba, S.-T. Myung, Tracking sodium cluster dynamics in hard carbon with a low specific surface area for sodium-ion batteries, Adv. Energy Mater. 14 (2024) 2304300.
[65] S.M. Nagmani, S. Puravankara, Hierarchically porous closed-pore hard carbon as a plateau-dominated high-performance anode for sodium-ion batteries, Chem. Commun. 60 (2024) 3071–3074.
[66] Y. Youn, B. Gao, A. Kamiyama, K. Kubota, S. Komaba, Y. Tateyama, Nanometer-size Na cluster formation in micropore of hard carbon as origin of higher-capacity Na-ion battery, NPJ Comput. Mater. 7 (2021) 48.
[67] L.K. Iglesias, E.N. Antonio, T.D. Martinez, L. Zhang, Z. Zhuo, S.J. Weigand, J. Guo, M.F. Toney, Revealing the sodium storage mechanisms in hard carbon pores, Adv. Energy Mater. 13 (2023) 2302171.
[68] A. Kamiyama, K. Kubota, D. Igarashi, Y. Youn, Y. Tateyama, H. Ando, K. Gotoh, S. Komaba, MgO-template synthesis of extremely high capacity hard carbon for Na-ion battery, Angew. Chem. Int. Ed. 60 (2021) 5114–5120.
[69] W. Song, Y. Tang, J. Liu, S. Xiao, Y. Zhang, Y. Gao, C. Yang, L. Liu, Mild pretreatment synthesis of coal-based phosphorus-doped hard carbon with extended plateau capacity as anodes for sodium-ion batteries, J. Alloys Compd. 946 (2023) 169384.
[70] X. Zhao, P. Shi, H. Wang, Q. Meng, X. Qi, G. Ai, F. Xie, X. Rong, Y. Xiong, Y. Lu, Y.-S. Hu, Unlocking plateau capacity with versatile precursor crosslinking for carbon anodes in Na-ion batteries, Energy Storage Mater 70 (2024) 103543.
[71] N. Shimizu, T. Mori, N. Igarashi, H. Ohta, Y. Nagatani, T. Kosuge, K. Ito, Refurbishing of small-angle x-ray scattering beamline, BL-6A at the photon factory, J. Phys. Conf. Ser. 425 (2013) 202008.
[72] H. Takagi, N. Igarashi, T. Mori, S. Saijo, H. Ohta, Y. Nagatani, T. Kosuge, N. Shimizu, Upgrade of small angle x-ray scattering beamline BL-6A at the photon factory, AIP Conf. Proc. 1741 (2016) 030018.
[73] N. Shimizu, K. Yatabe, Y. Nagatani, S. Saijyo, T. Kosuge, N. Igarashi, Software development for analysis of small-angle x-ray scattering data, AIP Conf. Proc. 1741 (2016) 050017.
[74] D. Orthaber, A. Bergmann, O. Glatter, SAXS experiments on absolute scale with Kratky systems using water as a secondary standard, J. Appl. Cryst. 33 (2000) 218–225.
[75] A.J. Allen, F. Zhang, R.J. Kline, W.F. Guthrie, J. Ilavsky, NIST standard reference material 3600: absolute intensity calibration standard for small-angle x-ray scattering, J. Appl. Cryst. 50 (2017) 462–474.
[76] G. Hasegawa, T. Deguchi, K. Kanamori, Y. Kobayashi, H. Kageyama, T. Abe, K. Nakanishi, High-level doping of nitrogen, phosphorus, and sulfur into activated carbon monoliths and their electrochemical capacitances, Chem. Mater. 27 (2015) 4703–4712.
[77] M. Hesse, H. Meier, B. Zeeh, Spectroscopic Methods in Organic Chemistry, Thieme, 2008 second ed.
[78] L. Xiao, H. Lu, Y. Fang, M.L. Sushko, Y. Cao, X. Ai, H. Yang, J. Liu, Low-defect and low-porosity hard carbon with high Coulombic efficiency and high capacity for practical sodium ion battery anode, Adv. Energy Mater. 8 (2018) 1703238.
[79] C. Fan, R. Zhang, X. Luo, Z. Hu, W. Zhou, W. Zhang, J. Liu, J. Liu, Epoxy phenol novolac resin: a novel precursor to construct high performance hard carbon anode toward enhanced sodium-ion batteries, Carbon N. Y. 205 (2023) 353–364.